Insights into the breakdown mechanism of anodic oxide film

Jiping Zhao,[1,2,‡] Yizhuo Li,[1,2,‡] Jie Zhu,[1,2] Jingyi An,[1,2] Xiangdong Ding,[3] and Youlong Xu[1,2,*,†]

[1] *Electronic Materials Research Laboratory, Key Laboratory of the Ministry of Education & International Center for Dielectric Research, Xi'an Jiaotong University, Xi'an 710049, China*

[2] *Shaanxi Engineering Research Center of Advanced Energy Materials & Devices, Xi'an Jiaotong University, No. 28, West Xianning Road, Xi'an 710049, China*

[3] *State Key Laboratory for Mechanical Behavior of Materials, Xi'an Jiaotong University, Xi'an 710049, China*

(Received 27 September 2023; revised 28 March 2024; accepted 15 May 2024; published 31 May 2024)

The breakdown mechanism of the anodic-oxide-film–electrolyte system has been studied for a long time, but there are still very few experimental studies that can summarize its physical image. Here, we report a finding on the breakdown mechanism of the tantalum (Ta) oxide-electrolyte system. We observe the evolution process of oxygen bubbles in Ta oxide films and demonstrate that oxygen generation is a cause of breakdown. The oxygen evolution reaction not only provides the initial electron injection for avalanche breakdown, but the resulting oxygen bubbles also lead to a concentration of stress and electric field. Further studies have shown that oxygen vacancies in oxide films are key to driving oxygen evolution and electron-current formation. Based on these findings, we attenuated oxygen evolution by the addition of a reducing agent, and the crystallization of the Ta oxide films was consequently drastically reduced, with the leakage current density of the dielectric being only 12.6% of the original. Therefore, this study not only contributes to an in-depth understanding of the breakdown mechanism of anodic oxide films, but also provides a promising prospect for the fabrication of high-quality Ta capacitors.

DOI: 10.1103/PhysRevApplied.21.054066

Dielectric-material-based capacitors are widely used in pulsed power equipment because of their high power density compared to electrochemical energy-storage devices [1–3]. Oxides of valve metals, such as Al, Ti, Nb, and Ta, are a very important class of dielectric materials [4]. Their dense film layers are the core components of electrolytic capacitors and play important roles in electronic circuits, such as bypassing, filtering, and coupling [5–7]. In the production of various types of electrolytic capacitors, the electrochemical anodic oxidation method is widely used because of its low cost, simple operation, and easy control [8]. The anodic oxide film is formed by exposing the metal anode to the electrolyte and then applying a voltage bias between the anode and the counter electrode. If the process is done properly, the resulting oxide film is usually homogeneous and amorphous, which is necessary to ensure the good electrical performance of electrolytic capacitors.

However, it is not an easy task to obtain a high-quality oxide film. This is because the amorphous oxide film is extremely unstable thermodynamically and can be broken down once a large external energy is applied. Breakdown is often accompanied by sparking and crystallization, or a combination of these, depending on the metal [9]. The oxides of Ta and Nb are particularly prone to crystallization. Excessive crystallization usually means failure of the tantalum capacitor and can even lead to equipment burnout and explosion, causing incalculable damage to electronic equipment [10–12]. As a result, engineers are extra careful when selecting tantalum capacitors as filter components, despite their excellent performance. Although breakdown can occur during the use of the capacitor, the initial defect is often formed during the anodizing process. Therefore, a deep and comprehensive understanding of the breakdown mechanism of anodic oxide films is required to avoid breakdown during manufacturing.

Research on the breakdown of anodic oxide films began in the 1950s. Vermilyea [13] and Jackson [14] introduced the concept of field crystallization and experimentally demonstrated that strong electric fields and high temperatures exacerbated the crystallization of oxide films. This discovery was later confirmed through many experiments and had a remarkably positive impact on the manufacture of anode films for Ta- and Nb-based capacitors. Yahalom and Zahavi put forward several valuable comments on the crystallization of oxide films, such as (a) the crystallization of oxide films may be related to the type and concentration of anions in the electrolyte, (b) the presence of large compressive stresses inside the oxide film during growth

*Corresponding author: ylxu@mail.xjtu.edu.cn
†Corresponding author: ylxuxjtu@mail.xjtu.edu.cn
‡Jiping Zhao and Yizhuo Li contributed equally to this work.

 © 2024 American Physical Society

promotes the development of crystallization, and (c) crystallization is a result of breakdown and is controlled by the oxide-electrolyte interface [15,16]. Subsequently, Sato derived a mathematical model of the compressive stress in the anodic oxide film generated by the electrostriction effect and interfacial tension from a thermodynamic point of view and concluded that this compressive stress was sufficient to cause mechanical stress breakdown of the oxide film [17]. Yang *et al*. observed the evolution of stresses and strains in Ta oxide films under strong electric fields, but they concluded that the compressive stresses came from multiple contributions [18,19]. Nevertheless, the biggest doubt in the theory lies in the inability to provide a reasonable explanation for the positive strain and positive stress in the oxide film [20]. A major breakthrough in the breakdown mechanism occurred in 1976 when Ikonopisov developed a mathematical model for the avalanche breakdown of Ta oxide films, which matched well with experimental observations [21]. The avalanche breakdown theory was further developed by Kadary *et al*. and applied to describe the breakdown behavior of aluminum oxide, again showing a great deal of realism [22,23]. Unfortunately, the model regarding the electrolyte for electron injection is considered based on the tight metallic contact in solid-state physics. In other words, the electrolyte in the model can emit electrons directly into the oxide film, which is obviously unreasonable. To explain this behavior, Christov speculated that the electrolyte could be modeled as a doped semiconductor that injected electrons into the oxide [9]. However, although such a model reproduces the functional form of the leakage current, it has no physical basis [24]. Albella *et al.* further developed the theory of avalanche breakdown by suggesting that the anions entering the interior of the oxide film could act as discharge centers and inject electrons released from impurities into the conduction band of the oxide film through a field-ionization mechanism, which, in turn, triggered avalanche breakdown [25–27]. The theory can reasonably explain the main features of the breakdown problem, i.e., the critical thickness of breakdown, the appearance of sparks, and the variation of breakdown voltage with electrolyte concentration. However, this hypothesis has not been confirmed by experiments. Since then, a few papers have been published on the study of anodic oxide films [28–31], but the breakdown mechanism has hardly been further developed.

This brief overview reveals that the underlying mechanism governing the breakdown phenomenon in metal-oxide-electrolyte systems is still controversial. In the broader context, it is still doubtful whether it is mechanical or electrical stress breakdown. Now first in assuming their reasonableness, there are still three specific issues in dispute. In summary, the main points are as follows. (i) Avalanche breakdown provides a good description of the breakdown mechanism in oxide films, but what is the source of the electrons injected into the oxide film from the electrolyte? (ii) It can be observed in the experiment that there are also obvious bumps or pits on the local surface of the oxide film [14,32]. This is clearly not explained by compressive stress, so what is the source of these defects? (iii) Numerous studies have shown that anions in solution penetrate deep into the oxide film [28,29,31], but what effect do they have on dielectric breakdown? Therefore, further research on the breakdown mechanism of Ta oxide films is necessary to give a clear answer to the above questions. Only in this way is it possible to suppress breakdown to the greatest extent possible from the root.

Here, we have conducted a comprehensive study of the morphology and surface properties of Ta anodic oxide films. Accordingly, an alternative viewpoint is proposed that can reasonably explain several doubts in the breakdown mechanism of anodic oxide films. Under the guidance of this theory, Ta pentoxide films with high quality were prepared.

I. RESULTS AND DISCUSSION

A. The discovery and demonstration of "oxygen crystallization"

In fact, Haring suggested as early as the 1950s that the crystallization of Ta oxide films might be related to the evolution of oxygen on the surface. He firmly states that "oxygen gas is evolved when film breakdown occurs" [33]. However, numerous academic sources indicate that the formation efficiency of Ta is almost close to 100%, which means that oxygen bubbles are difficult to observe [34,35]. It was not until 2011 that Hammer *et al*. once again reported this phenomenon, which contradicted the literature, that "a large amount of oxygen was found to be evolved from the anode during the manufacturing process of electrolytic capacitors" [36]. Their results show that the formation of visible oxygen bubbles requires a current density of >1 mA cm^{-2}. Therefore, to further amplify this phenomenon, we chose a current density of 10 mA cm^{-2} for anodic oxidation in 0.1-wt % H_2SO_4 and H_3PO_4 solutions at 85 °C. Figures S1(a), S1(b), S1(d), and S1(e) within the Supplemental Material record the real-time scenes when the voltage has just reached 35 V and after holding at 100 V for 20 min [37]. It can be seen that there are more bubbles on the surface of the sample in sulfuric acid than in phosphoric acid during the whole anodic oxidation process. Figures 1(a)–1(d) show SEM photographs of the surface and cross section of the oxide films obtained in sulfuric acid and phosphoric acid. Small white dots or particles can be seen distributed on the dark gray substrate. Raman spectroscopy analysis [37] shows that this is a sign of crystallization of the Ta_2O_5 film (see Fig. S2 within the Supplemental Material [37]). In addition, a large number of circular dimples can be seen distributed on the surface of the sample in Fig. 1(a), while

there are few dimples in Fig. 1(b). These features have also been observed in previous studies [14,32], but there is no explanation for their formation. Interestingly, we found that the number of both crystalline spots and circular dimples was proportional to the rate of oxygen precipitation from the sample surface during the anodizing process. Therefore, this suggests that there may be a correlation between the yield of oxygen bubbles and the crystallization of the oxide film. Fortunately, we did observe oxygen bubbles in the cross sections of the Ta oxide films obtained in both sulfuric acid and phosphoric acid, and the number of oxygen bubbles in the former was much higher than in the latter, which was consistent with what was observed for anodic oxidation. Notably, the location of some oxygen bubbles corresponds to the location of dimples and crystallites, suggesting that it may be the oxygen bubbles that are responsible for these defects.

To further verify our inference, the following experiments were designed to investigate this from both positive and negative perspectives. A 0.1-wt % aqueous phosphoric acid solution was chosen as the electrolyte for the anodic oxidation at room temperature (∼25 °C).

(i) A strong antioxidant, citric acid (CA), of 10 m*M* is added to the electrolyte to minimize the oxidation of adsorbed O^{2-} to oxygen. If the crystallization on the surface weakens as the oxygen bubble in the Ta oxide film decreases, this indicates that crystallization is the result of oxygen evolution.

(ii) Adding 10 m*M* of the strong oxidizing agent H_2O_2 to the electrolyte serves to produce more oxygen under electrolytic conditions. If the number of oxygen bubbles in the Ta oxide film becomes larger and the number of crystallization sites on the surface increases with the oxygen bubbles, this again proves that the evolution of oxygen causes crystallization.

Figure 2(a) shows a cross section of the anodic oxide film of Ta in 0.1-wt % H_3PO_4 at 100 V. It can be seen that there are more defects on the external surface of the oxide film and the number of oxygen bubbles on the cross section is high. However, the surface of the anodized film with CA added is very clean and hardly any crystallization points are visible [see Figs. 2(b) and 2(e)]. More importantly, there are no oxygen bubbles inside the oxide film. On the contrary, the oxide film with the addition of H_2O_2 has a large number of oxygen bubbles inside and crystallization on the external surface is more serious [Figs. 2(c) and 2(f)]. The above results indicate that crystallization becomes more intense with an increasing number of oxygen bubbles and diminishes with a decreasing number of oxygen bubbles, suggesting that it is indeed the evolution of oxygen that leads to crystallization. To this end, we have identified and demonstrated that oxygen bubbles are a key trigger for the crystallization of Ta anode oxide films, which has not been mentioned in previous studies. Therefore, this crystallization mechanism is referred to as "oxygen crystallization" in this paper.

B. Mechanisms of stress and strain generation

Understanding the evolution of oxygen bubbles is crucial to explain the crystallization of Ta oxide films,

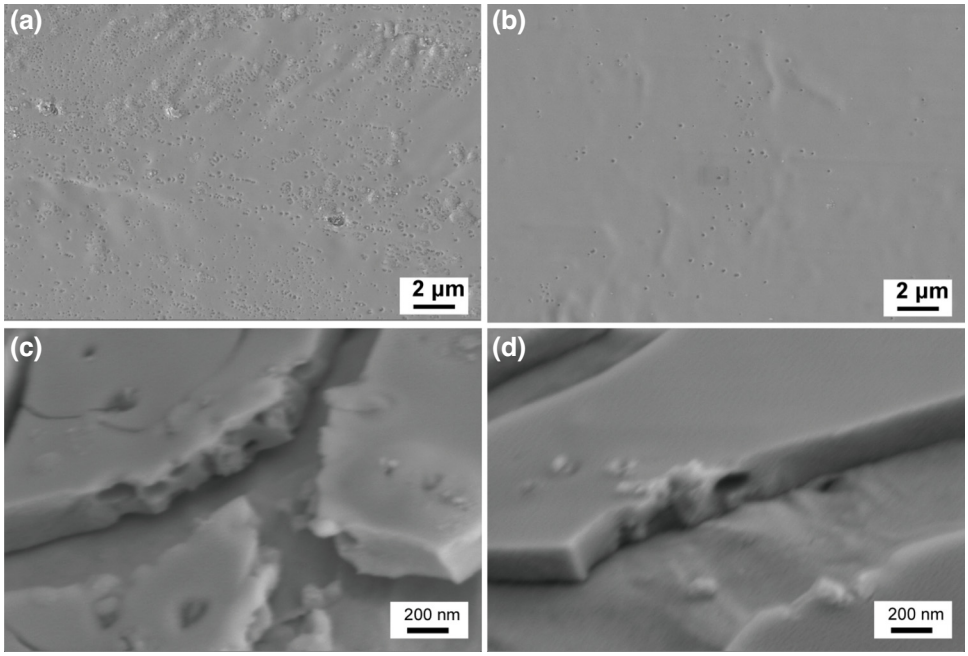

FIG. 1. Surface and cross-section morphology of the samples after holding at 85 °C for 20 min at 100 V in 0.1-wt % sulfuric acid (a),(c) and phosphoric acid (b),(d).

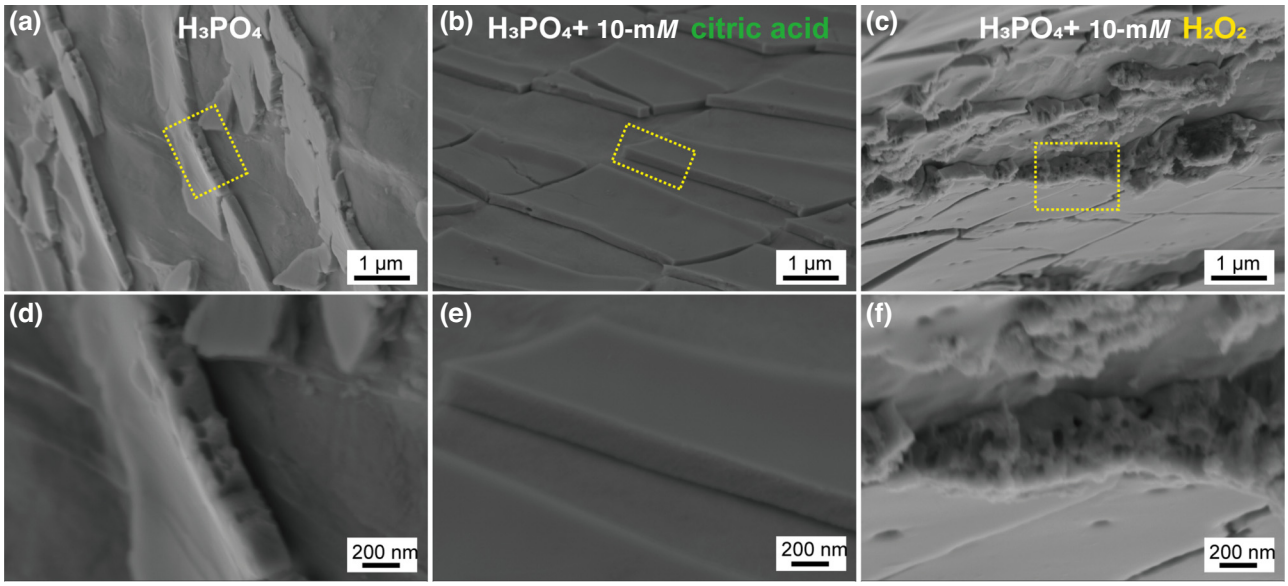

FIG. 2. Cross sections after anodic oxidation in 0.1-wt% H_3PO_4 solution [(a),(d)], 0.1-wt% H_3PO_4 + 10-m*M* CA [(b),(e)], 0.1-wt% H_3PO_4 + 10-m*M* H_2O_2 [(c),(f)] at 25 °C for 30 min at 100 V.

as it is closely related to the surface morphology of the oxide film (bumps and pits). Therefore, we monitored the different stages of the anodic oxidation process of Ta at 100 V. Figure 3(a) shows the cross-section shape of the Ta oxide film when it first reaches 30 V. No oxygen bubbles were present in the interior of the oxide film and no crystallization was found on the surface of the oxide film. The oxide film becomes thicker when the voltage reaches 60 V, but still no oxygen bubbles and crystallization are seen [Fig. 3(b)]. As the oxide film continued to thicken, an olive-shaped oxygen bubble with a length of about 150 nm was found in Fig. 3(c). As can be seen from the inset in Fig. 3(c), there is still no defect generation on the oxide film surface, probably because the oxygen bubbles are too small and far from the surface. Figure 3(d) shows that, as the oxidation time increases, the oxygen bubble becomes larger and closer to the outer side of the oxide film. It is noteworthy that at this moment a small number of crystalline spots and circular dimples are shown in the illustration of Fig. 3(d). It can be inferred that this may be due to the further enlargement of the oxygen bubble. The information in Fig. 3(e) then directly verifies our inference. It can be seen that the size of the oxygen bubble is already around 200 nm and very close to the outer side of the oxide film, so that the dimples are visible to the naked eye. In addition to the pits, a significant positive strain on the oxide film surface, i.e., bulging, as described above, can be observed in the inset of Fig. 3(e). Particularly noteworthy are the obvious air pores in the region where positive strain is generated. It is not difficult to speculate that this is the result of oxygen-bubble rupture.

Figure 3(f) provides us with more visual evidence. It can be seen that most of the oxygen bubbles have ruptured and left defects, such as pores, cracks, and bumps, on the surface.

Interestingly, crystallization around the gas pores is more severe, as can be seen in the illustration. When the constant-voltage duration is extended to 60 min, the oxide film undergoes rather severe crystallization (Fig. S3 within the Supplemental Material [37]). However, channels left by oxygen-bubble evolution are still observed in the crystalline film [see Fig. 3(g)].

Therefore, it can be concluded that the surface defects observed in previous studies, such as positive strain and dimples, as well as crystallization, are all related to the evolution of oxygen bubbles. It is important to recognize that both dimples and bulges seen on the surface of the oxide film indicate the presence of significant stresses within the oxide film. Previous studies have shown that, for aluminum oxide films, the internal pressure of an oxygen bubble with a radius of 20 nm can be as high as 100 MPa [44]. Similar results were obtained within anodic oxide films of aluminum-copper alloys [45]. Based on this, we can deduce that for those bubbles with an internal pressure greater than the surface tension of the oxide film it is easy to form a bulge or even directly lead to the breakage of the oxide film [as shown by oxygen-bubble *b* in Fig. 3(h)]. While for those oxygen bubbles that are close to the surface and the internal pressure is lower than the surface tension of the oxide film, they are most likely to form dimples [as shown by oxygen-bubble *c* in Fig. 3(h)]. However, for those oxygen bubbles that are far from the oxide film (bubble *a*), the internal pressure is likely to be

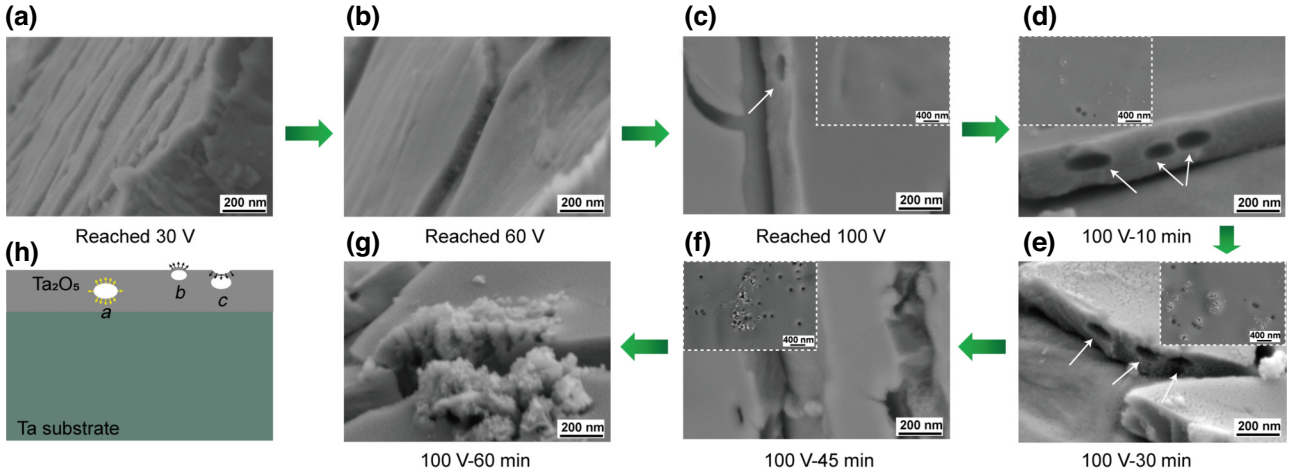

FIG. 3. Cross-section morphology of anodic oxide film at different stages during the process of voltage rising to 100 V in 0.1-wt % H_3PO_4 solution at 85 °C: (a) reached 30 V; (b) reached 60 V; (c) reached 100 V; holding at 100 V for (d) 10 min, (e) 30 min, (f) 45 min, and (g) 60 min. (h) Schematic diagram of the oxygen bubble in different states.

equal to the surface tension of the oxide film and it will not exhibit significant strain.

In addition to creating stress within the oxide film, the presence of oxygen bubbles may also cause a concentration of electric fields (which is described in Sec. I C [Figs. 5(i)–5(j)]). This is because the thickness of the oxide film is less than the average thickness in the presence of oxygen bubbles, where the electric field strength is more concentrated at the same voltage. As a result, the area with oxygen bubbles acts as a concentration of both electric field and stress and is more likely to have breakdown. Therefore, the breakdown of the Ta oxide film should be a coupling of stress breakdown and avalanche breakdown.

C. Origin of injected electrons in avalanche breakdown

To elucidate the origin of injected electrons in the avalanche-breakdown mechanism, it is necessary to further investigate the mechanism of oxygen-bubble generation. Figures 4(a) and 4(b) show the cross sections of the Ta oxide films at different locations after the voltage is held at 100 V for 30 min. Two oxygen bubbles with a diameter of about 200 nm can be seen in Fig. 4(a). Based on the size of the oxygen bubble, it can be determined that the bubble has been formed for some time. However, another oxygen bubble in Fig. 4(b) is much smaller (∼50 nm). This suggests that the formation of oxygen bubbles in the oxide film is most likely not simultaneous. In addition, we know that the anodic-oxide-film–electrolyte interface is not fixed but growing during the anodic oxidation process. Therefore, combined with the location of the two bubbles in the oxide film, we can infer that oxygen bubbles may be continuously generated at the new oxidation-film–electrolyte interface. To facilitate understanding, we give a diagram of oxygen-bubble generation in Fig. 4(c). Once oxygen bubbles appear at the newly grown interface, they isolate the entry of the electrolyte and eventually form inclusions within the oxide film. It is undeniable that oxygen bubbles may also form at the metal-oxide–film interface. We did also find a small number of bubbles of this type characterized by a pronounced rising trailing tail (shown in Fig. S4 within the Supplemental Material), which was quite different from the type of bubbles we studied [37]. Interestingly, as can be seen in Fig. 1(c), oxygen bubbles are distributed at different heights along the oxide film. These results suggest that the oxide-film–electrolyte interface has an important influence on the formation of oxygen bubbles. Also, it is important to mention that Fig. 1 shows more oxygen bubbles in the oxide film grown in sulfuric acid than in phosphoric acid. This suggests that the anion may also have an important effect on the physical and chemical properties of the oxide-film–electrolyte interface.

To further investigate the interfacial properties of the anodic oxide films, XPS measurements were performed on Ta anodic oxide films grown in sulfuric acid and phosphoric acid. Figures 5(a) and 5(c) show the typical XPS results for the Ta 4*f* core level of the oxide films obtained in sulfuric acid and phosphoric acid, respectively. Ta 4*f* 7/2 and Ta 4*f* 5/2 peaks appear at 26.2 and 28.0 eV, respectively, indicating the existence of Ta species in the form of Ta^{5+} [Fig. 5(a)] [46–50]. In addition, the characteristic peaks of Ta^{4+} can be seen at 25.7 and 27.8 eV, indicating the presence of small amounts of low-valent Ta oxides. The oxide films obtained in sulfuric acid show similar spectra, but the area of the characteristic peaks representing Ta^{4+} is more dominant, indicating that the Ta oxide contains more oxygen vacancies (O-*V*) [51]. More information about the oxygen vacancies can be obtained by analyzing the XPS spectra of O in Figs. 5(b) and 5(d).

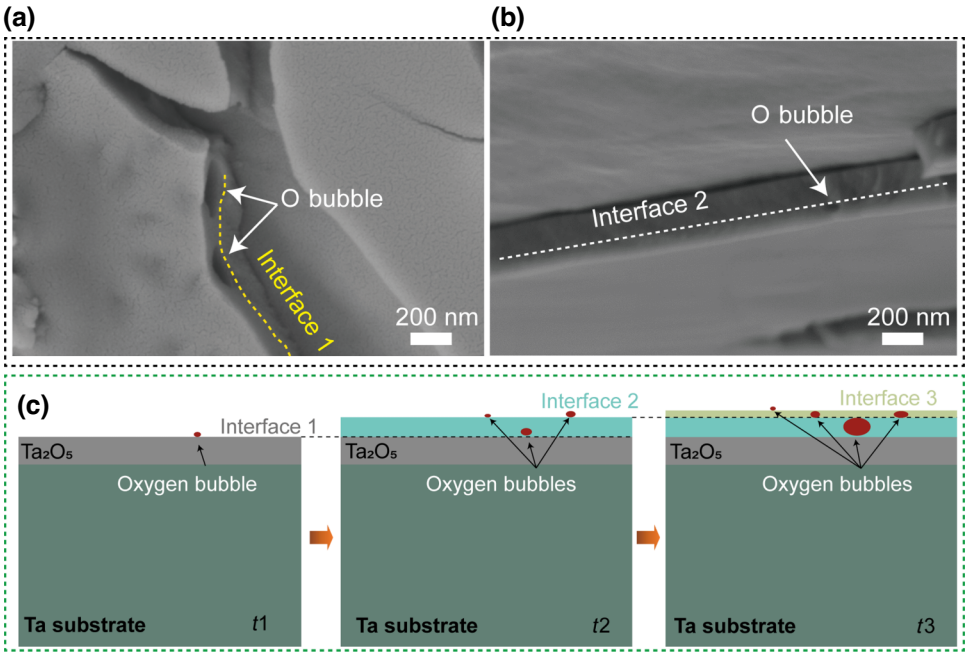

FIG. 4. Oxygen bubbles observed at different locations in the same oxide film after holding at 85 °C at 100 V for 30 min: (a) close to the outer side of the oxide film, (b) far from the outer side of the oxide film. (c) Schematic diagram of the evolution of the oxide-film–electrolyte interface.

The O 2*p* orbitals show four XPS peaks at 530.3, 531.0, 532.0, and 533.2 that can be attributed to lattice oxygen, O vacancies, sulfate, and adsorbed oxygen on the surface, respectively [47,48] [Fig. 5(b)]. The XPS results for the O 2*p* orbitals shown in Fig. 5(d) are similar to the former, except that the lattice oxygen is shifted by 0.2 eV toward the high-binding energy and the peak of O-V is weaker. This indicates that the O-V concentration in the Ta oxide film obtained in phosphoric acid is lower. In addition, Figs. S5(a) and S5(b) within the Supplemental Material show the XPS peaks of sulfate and phosphate, which indicate that sulfate and phosphate are indeed present in the oxide film and chemically bonded to it [37]. The presence of O-V was further verified by electron paramagnetic resonance (EPR) spectra [Fig. 5(e)]. It can be seen that the oxide film prepared in sulfuric acid shows a strong EPR signal at $g = 2.003$, demonstrating the rich oxygen defects in the Ta oxide film [39]. It is important to note here that these oxygen defects are shown to be most likely oxygen vacancies occupied by one electron (denoted by V_o^+) [52]. However, the EPR signal of the oxide film obtained in phosphoric acid is weaker, indicating a lower content of V_o^+. Figure 5(f) shows the UV-vis absorption spectra of both oxide films. The absorption peaks located in the 300–400 cm^{-1} range are attributed to the excitation of electrons trapped in V_o^+ within the oxide film. The two absorption peaks in the visible range are due to the color of the oxide film itself and the interference effect of light [53–58]. It is of interest that the UV-absorption spectrum of the oxide film prepared in sulfuric acid undergoes a significant redshift compared to that obtained in phosphoric acid. This indicates that the band gap of the Ta oxide film prepared in phosphoric acid is higher. From a solid-state physics perspective, materials with high band gaps tend to require larger breakdown field strengths. Furthermore, the electrochemical impedance spectroscopy (EIS) results in Fig. 5(g) show that the Ta oxide film obtained in sulfuric acid has a smaller charge-transfer resistance (R_p) due to the presence of more V_o^+ within the oxide film.

In addition, we analyzed the thermal stability of both oxide films. Since Ta oxide films are difficult to peel off, the samples used for thermogravimetric (TG) and differential scanning calorimetry (DSC) testing are Ta foils with an anodic oxide film covering the surface. In other words, the sample consists of a Ta oxide film on the outside and a Ta core on the inside. If the oxide film is rich in V_o^+, oxygen from the environment will bind more easily to the Ta core at high temperatures, leading to an increase in sample mass. From Fig. 5(h), it can be seen that the mass of the sample prepared in sulfuric acid begins to increase at lower temperatures (~650 °C), which further proves that its V_o^+ content is higher. Clearly, all of the above results indicate that the Ta pentoxide films prepared by anodic oxidation contain V_o^+, and that the Ta oxide films obtained in phosphoric acid contain fewer V_o^+. Therefore, it is not difficult to understand that it is the presence of V_o^+ that promotes the production of oxygen bubbles. After all, numerous studies on the theory of electrochemical catalysis have shown that V_o^+ in substances can act as catalytic centers to promote oxygen evolution reactions [59–63]. The

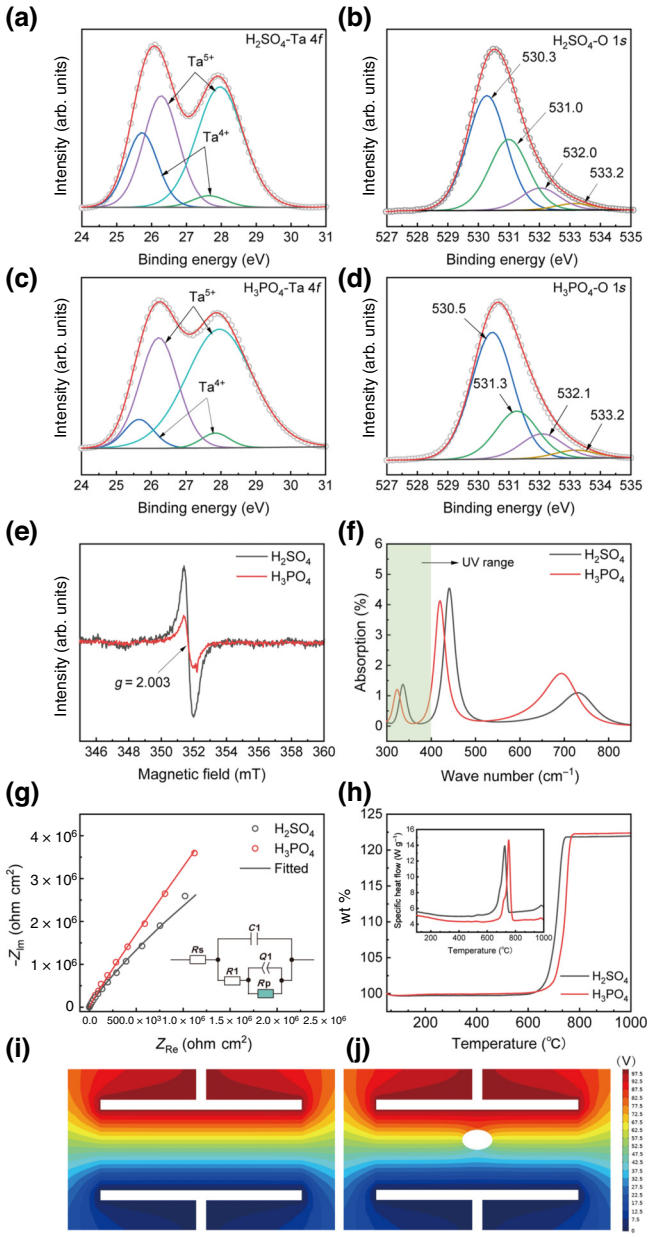

FIG. 5. Oxide films obtained in 0.1-wt % H_2SO_4 solution and 0.1-wt % H_3PO_4 maintained at 100 V for 30 min at 85 °C. XPS of Ta 4*f* (a),(c), O 1*s* (b),(d); EPR spectra (e); UV-vis absorption curves (f); EIS (g); TGA-DSC curves (h); simulations of the potential distribution in a perfect dielectric (i) and in a dielectric with oxygen bubbles (j).

electrons released from the oxygen ions to the oxide film are the main source of injected electrons in the avalanche breakdown.

To explore the effect of oxygen bubbles on the potential distribution, we performed numerical simulations using finite-element software (COMSOL). A metal-insulator-metal (*M-I-M*) structure was used instead of the metal-insulator-electrolyte system. The model was built based on the SEM cross section with a voltage of 100 V applied to the top edge and the bottom edge was grounded. The dielectric constant was set to 27. See Fig. S6 within the Supplemental Material for specific information on the *M-I-M* model [37]. As can be seen from Fig. 5(i), the electric potential distribution in the perfect dielectric is quite uniform. However, once oxygen bubbles form in the oxide film, they cause a steep increase in the local electric potential [Fig. 5(j)]. As a result, the initial injected electrons are accelerated and multiplied by the localized strong electric field, which, in turn, induces an avalanche breakdown of the dielectric.

D. Effect of anions on oxygen vacancies

From the discussion in the previous section, it was found that different anions led to different concentrations of oxygen vacancies. To explain this behavior, we calculated the HOMO and LUMO of three major species (a detailed discussion of ion types and contents is provided in Table S1 within the Supplemental Material [37]) present in solution, as shown in Fig. 6(a). It can be seen that the HOMO of all three species is distributed on an oxygen atom with no proton attached, indicating that the oxygen atom is a donor of electrons. Importantly, the HOMO energy of the three species is $SO_4^{2-} > H_2PO_4^- > H_3PO_4$, indicating that SO_4^{2-} has a stronger ability to donate electrons to the surface. Furthermore, it has been shown that the Fermi-energy level (relative to the vacuum-energy level) of Ta_2O_5 is −4.25 eV [64]. However, taking into account the oxygen vacancy, we assume that the Fermi-energy level rises by 0.3 eV to −3.95 eV [51]. Thus, the Fermi-energy level of Ta_2O_5 is much lower than the HOMO-energy level of the three species. According to the frontier molecular orbital theory [65,66], charge will be transferred from the HOMO of the adsorbate to the empty orbitals

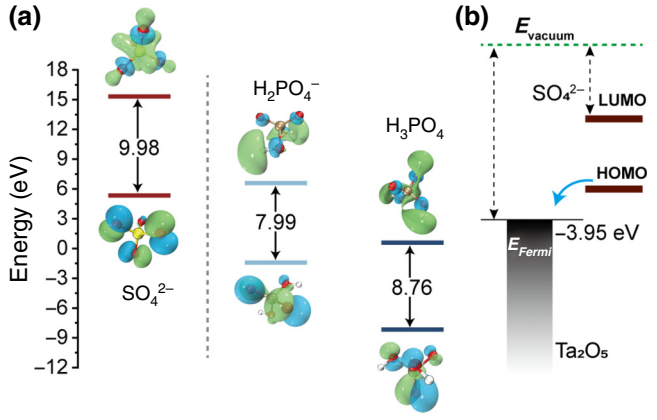

FIG. 6. (a) HOMO, LUMO, and energy gaps of SO_4^{2-}, $H_2PO_4^-$, and H_3PO_4. (b) Schematic illustration of the Fermi energy levels of the Ta oxide film relative to the HOMO-LUMO energy levels of SO_4^{2-}.

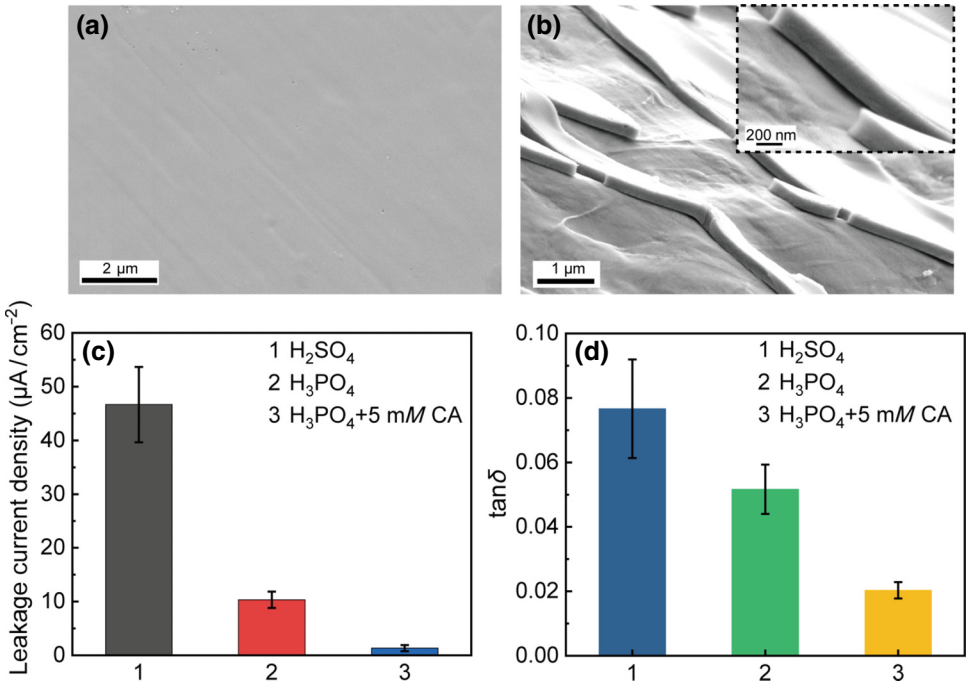

FIG. 7. Microscopic morphology of (a) surface and (b) cross section of 100-V Ta anodic oxide films prepared after the addition of 5-m*M* CA to 0.1-wt % H_3PO_4 solution at 85 °C; (c) leakage current density and (d) tanδ of the oxide films prepared in the three electrolytes.

(Ta 5*d*) of Ta_2O_5. To depict this mechanism more clearly, a schematic diagram is drawn, as shown in Fig. 6(b). Apparently, charge transfer from SO_4^{2-} to Ta 5*d* orbitals is easier because of its higher HOMO energy. As a result, the valence state of Ta is lower in the Ta oxide film obtained in 0.1-wt % sulfuric acid solution.

E. Anodizing process improvement

Based on the above theoretical analysis, we recognize that oxygen bubbles are an important cause of dielectric breakdown. Therefore, it is necessary to avoid the generation of oxygen bubbles in the growth of the anodic oxide film. CA is a strong reducing agent that prevents oxygen ions from being oxidized to oxygen. It can be seen from Figs. 7(a) and 7(b) that, despite anodic oxidation at high temperature and high current density, the oxide film shows almost no crystallization; this is attributed to the reduction of oxygen bubbles. Furthermore, Fig. 7(c) shows that sample 3 has the lowest leakage current density, which is only 2.8% of sample 1 and 12.6% of sample 2. The value of tanδ for sample 3 is only 0.02, which is much lower than those of samples 1 and 2, indicating that its oxide film is of good quality, as seen in Fig. 7(d). Therefore, the view of the breakdown mechanism of oxide films presented in this work is valid and will have a wide impact on the high-quality preparation of anodic oxide films of valve metals.

II. CONCLUSIONS

We found that the oxygen bubbles generated at the oxide-film–electrolyte interface during the anodic oxidation process were an important cause of the crystallization of Ta oxide films. The validity of this theory is mainly attributed to its ability to give reasonable answers to some of the main questions regarding the breakdown mechanism of the oxide film. First, our study shows that the Ta oxide film contains enough oxygen vacancies that their presence induces the release of electrons from the oxygen ions in the electrolyte to the oxide-film interface, thus generating oxygen. This process reasonably explains the origin of the injection electrons in the avalanche-breakdown mechanism. Second, the oxygen bubble has a large internal pressure, which is sufficient to be a source of internal stress in the oxide film. Therefore, the macroscopic strain of the oxide film can be attributed to the coupling of the internal pressure and surface tension of the oxygen bubble. Third, anions exhibit different reducibility, depending on their HOMO energies, which could explain the differences in the concentration of oxygen vacancies in Ta oxide films obtained in different electrolytes. Thus, our work opens an alternative perspective for the study of breakdown mechanisms of anodic oxide films. Nevertheless, some factors that have a significant effect on the electronic structure of solids, such as amorphous states, electric fields, and anion entry, have not been considered at the theoretical level of this work and will be the focus of future work.

III. METHODS

A. Specimen preparation

The Ta foil used in this work has a purity of 99.95% and a thickness of 30 μm, and it was purchased from Nanfang Tantalum Niobium Co. Ltd. Ta foil was cut into 1-cm^2 squares and spot-welded with 3-cm Ta wire as a handle for operation. The welded Ta electrodes (small Ta foil with handle) were ultrasonically cleaned in deionized water, alcohol, and acetone for 10 min, and finally rinsed with deionized water and placed in a vacuum oven (60 °C). To ensure the uniformity of the flatness of the Ta electrode, the Ta electrode was chemically polished in a mixture of hydrofluoric acid (HF) and nitric acid (HNO_3) (analytical grade, volume ratio of 2:5) for 1–2 min before use. The polished Ta electrode was carefully cleaned with deionized water before anodizing. The anodic oxidation process was carried out under constant current followed by constant-voltage mode; the voltage was set to 100 V and the constant-voltage time was generally 30 min if not specified. All anodic oxidation processes were based on a two-electrode system, in which the anode was a Ta electrode and the cathode was a platinum sheet with an area of 8 cm^2. The electrolytes used in the experiments were aqueous solutions of sulfuric acid (H_2SO_4) and phosphoric acid (H_3PO_4) (analytical grade). The dc power supply (model TN-XXZ02 DC) provided the required constant voltage.

B. Electrical performance measurements

All withstanding voltage and leakage current tests were performed on the TV-3CH instrument model (Yangzhou Baoou Electronics Co., Ltd., Yangzhou, China). The test conditions were as follows: the charging current density was 0.2 mA cm^{-2}, the maximum charging time allowed was 180 s, leakage current testing was performed at an applied voltage of 90 V (90% of the formation voltage), and the test duration was 180 s. The electrolyte used in all withstand voltage and leakage current tests was a 0.1-wt % phosphoric acid aqueous solution with a temperature of approximately 25 °C. An *LCR* meter (KEYSIGHT E4980AL) was used to measure the capacitance density (C) and the dissipation factor ($\tan\delta$) at a fixed frequency of 100 Hz. The test solution used was a 30-wt % aqueous solution of sulfuric acid. The above electrical parameters were measured according to the group standard of the China Electronic Components Industry Association. EIS was performed using the Versatile Multichannel Potentiostat 2/Z (VMP2, Princeton Applied Research) electrochemical workstation. All electrochemical tests were performed in a three-electrode system with a saturated calomel electrode as the reference electrode and a platinum sheet as the counter electrode. To avoid the effect of chloride ions on the oxide film, we connected the reference electrode to the test solution using a salt bridge filled with 0.1-wt % H_3PO_4 solution. To reduce the effect of solution resistance, the distance between the Luggin capillary (salt bridge) and the working electrode is about 1–2 mm, which is slightly larger than the outer diameter of the Luggin capillary [6]. EIS data were obtained in the frequency range between 100 kHz and 0.1 Hz with an ac signal with a potential amplitude of 10 mV as a perturbation.

C. Characterization

Field-emission SEM (model S4800) was used to observe the microscopic morphology [extra high tension (EHT) = 5 kV, working distance (WD) = 8.6 mm, signal A = SE2] of the Ta anodic oxide film. XPS data were collected on a Thermo Fisher ESCALAB Xi instrument. The spectra were fitted using Gaussian and hybrid Gaussian-Lorentzian functions. The peak positions were then calibrated to the C 1*s* peak at 284.8 eV. The reflection and absorption spectra were measured on a PE Lambda950 UV–Vis–near-IR spectrophotometer. The EPR spectra (A300-9.5/12) were obtained at a microwave frequency of 9.86 GHz at 300 K. The thermal stability of three oxide films was analyzed by TGA and DSC (METTLER TOLEDO, Greifensee, Switzerland).

D. Computational details

In this work, the highest occupied molecular orbitals (HOMOs) and lowest unoccupied molecular orbitals (LUMOs) for three species were obtained using the Gaussian09 program code [67]. The geometries of the molecules were optimized using the B3LYP density functional and the 6-31G(d) orbital basis set. The HOMOs and LUMOs were analyzed using the Multiwfn package [68] and Visual Molecular Dynamics program [69].

ACKNOWLEDGMENTS

This work is supported by the Natural Science Foundation of China (Grant No. 62374132), the National Key Research and Development Program of China (Grant No. 2022YFE0122500), the 55th Research Institute of China Electronics Technology Group Corporation (2022 open fund 82), and the Science and Technology on Monolithic Integrated Circuits and Modules Laboratory (Grant No. 61428032203). The authors also appreciate the Instrumental Analysis Center of XJTU for sample testing and technical assistance.

Jingyi An, Yizhuo Li, Jiping Zhao, and Jie Zhu analyzed data; Xiangdong Ding provided the code for the calculation; Yizhuo Li and Jiping Zhao carried out the experiments and collected the data; Youlong Xu and Jiping Zhao designed the project and wrote the manuscript. All authors discussed the results and commented on the manuscript.

The authors declare no conflict of interest.

[1] L. Xu, T. Meng, X. Zheng, T. Li, A. H. Brozena, Y. Mao, Q. Zhang, B. C. Clifford, J. Rao, and L. Hu, Nanocellulose-carboxymethylcellulose electrolyte for stable, high-rate zinc-ion batteries, Adv. Funct. Mater. **33**, 2302098 (2023).

[2] L. Xu and C. V. Thompson, Mechanisms of the cyclic (de)lithiation of RuO_2, J. Mater. Chem. A **8**, 21872 (2020).

[3] L. Xu, M. J. Chon, B. Mills, and C. V. Thompson, Mechanical stress and morphology evolution in RuO_2 thin film electrodes during lithiation and delithiation, J. Power Sources **552**, 232260 (2022).

[4] G. Tranchida, A. Zaffora, F. Di Franco, and M. Santamaria, The effect of anodizing bath composition on the electronic properties of anodic Ta-Nb mixed oxides, Nanomaterials (Basel) **12**, 1 (2022).

[5] J. Zhao, Y. Xu, W. Hou, Y. Li, and X. Ding, An ultra-thin, ultra-high capacitance density tantalum capacitor for 3D packaging, Adv. Mater. Technol. **8**, 2201967 (2023).

[6] J. Zhao, Y. Xu, Z. Sun, and X. Yao, Morphological evolution of corrosion pits on the (200) and (211) surfaces of tantalum foil, J. Electrochem. Soc. **170**, 021504 (2023).

[7] R. G. Spurney, H. Sharma, P. M. Raj, R. Tummala, N. Lollis, M. Weaver, M. Romig, S. Gandhi, and H. Brumm, 3-D packaging and integration of high-density tantalum capacitors on silicon, IEEE Trans. Compon., Packag., Manuf. Technol. **9**, 1466 (2019).

[8] M. M. Momeni, M. Mirhosseini, M. Chavoshi, and A. Hakimizade, The effect of anodizing voltage on morphology and photocatalytic activity of tantalum oxide nanostructure, J. Mater. Sci.: Mater. Electron. **27**, 3941 (2015).

[9] S. G. Christov, Electronic currents in anodic polarization of oxide-covered valve metals, J. Electroanal. Chem. Interfacial Electrochem. **105**, 275 (1979).

[10] J. S. T. Zednicek and H. Leibovitz, A study of field crystallization in tantalum capacitors and its effect on DCL and reliability, CARTS USA (2009).

[11] Y. Freeman, P. Lessner, and I. Luzinov, Reliability and failure mode in solid tantalum capacitors, ECS J. Solid State Sci. Technol. **10** (2021).

[12] J. Virkki and S. Tuukkanen, Testing the effects of temperature cycling on tantalum capacitors, Microelectron. Reliab. **50**, 1121 (2010).

[13] D. A. Vermilyea, Nucleation of crystalline Ta_2O_5 during field crystallization, J. Electrochem. Soc. **104**, 542 (1957).

[14] N. F. Jackson, Field crystallization of anodic films on tantalum, J. Appl. Electrochem. **3**, 91 (1972).

[15] J. Yahalom and J. Zahavi, Experimental evaluation of some electrolytic breakdown hypotheses, Electrochim. Acta **16**, 603 (1971).

[16] J. Yahalom and J. Zahavi, Electrolytic breakdown crystallization of anodic oxide films on Al, Ta and Ti, Electrochim. Acta **15**, 1429 (1970).

[17] N. Sato, A theory for breakdown of anodic oxide films on metals, Electrochim. Acta **16**, 1683 (1971).

[18] L. Yang, M. Viste, J. Hossick-Schott, and B. W. Sheldon, Internal stress evolution during field-induced crystallization of anodic tantalum oxide, Electrochim. Acta **81**, 90 (2012).

[19] L. Yang, M. Viste, J. Hossick-Schott, and B. W. Sheldon, Understanding internal stress evolution mechanisms associated with field crystallization of anodic tantalum oxide, J. Eelectroceram. **32**, 108 (2013).

[20] J. L. Ord, Electrostriction in anodic oxides: Comparison with macroscopic theory, J. Electrochem. Soc. **127**, 2682 (1980).

[21] S. Ikonopisov, Theory of electrical breakdown during formation of barrier anodic films, Electrochim. Acta **22**, 1077 (1977).

[22] V. Kadary and N. Klein, Electrical breakdown: I. During the anodic growth of tantalum pentoxide, J. Electrochem. Soc. **127**, 139 (1980).

[23] N. Klein, V. Moskovici, and V. Kadary, Electrical breakdown: II. During the anodic growth of aluminum oxide, J. Electrochem. Soc. **127**, 152 (1980).

[24] V. G. Bordo and T. Ebel, First-principles theory of electrical breakdown in barrier anodic films in contact with an electrolyte, Electrochim. Acta **354**, 136490 (2020).

[25] J. M. Albella, I. Montero, and J. M. Martinez-Duart, A theory of avalanche breakdown during anodic oxidation, Electrochim. Acta **32**, 255 (1987).

[26] I. M. J. M. Albella and J. M. Martinez-Duart, Dielectric breakdown processes in anodic Ta_2O_5 and related oxides, J. Mater. Sci. **26**, 3422 (1991).

[27] J. M. Albella, I. Montero, and J. M. Martinez-Duart, Electron injection and avalanche during the anodic oxidation of tantalum, J. Electrochem. Soc. **131**, 1101 (1984).

[28] J. D. Sloppy, D. D. Macdonald, and E. C. Dickeyz, Growth laws of bilayer anodized tantalum oxide films formed in phosphoric acid, J. Electrochem. Soc. **157**, C157 (2010).

[29] Y.-H. Kim and K. Uosaki, Preparation of tantalum anodic oxide film in citric acid solution - evidence and effects of citrate anion incorporation, J. Electrochem. Sci. Technol. **4**, 163 (2013).

[30] S. Ono, K. Kuramochi, and H. Asoh, Effects of electrolyte pH and temperature on dielectric properties of anodic oxide films formed on niobium, Corros. Sci. **51**, 1513 (2009).

[31] J. D. Sloppy, Z. Lu, E. C. Dickey, and D. D. Macdonald, Growth mechanism of anodic tantalum pentoxide formed in phosphoric acid, Electrochim. Acta **87**, 82 (2013).

[32] Salvatore Piazza, Francesco Di Quarto, and C. Sunseri, Breakdown phenomena during the growth of anodic oxide films on zirconium metal: Influence of experimental parameters on electrical and mechanical breakdown, J. Electrochem. Soc. **131**, 2901 (1984).

[33] H. E. Haring, The mechanism of electrolytic rectification, J. Electrochem. Soc. **99**, 30 (1952).

[34] O. Kerrec, D. Devilliers, H. Groult, and M. Chemla, Dielectric properties of anodic oxide films on tantalum, Electrochim. Acta **40**, 719 (1995).

[35] L. Young, Anodic oxide films on tantalum electrodes part 1. Thickness and current efficiency of formation, Trans. Faraday Soc. **50**, 153 (1953).

[36] C. Hammer, B. Walther, H. Karabulut, and M. M. Lohrengel, Oscillating oxygen evolution at ta anodes, J. Solid State Electrochem. **15**, 1885 (2011).

[37] See the Supplemental Material at http://link.aps.org/supplemental/10.1103/PhysRevApplied.21.054066 for photographs of oxygen evolution during anodic oxidation,

Raman spectra, XPS analysis of S 2*p* and P 2*p*, simulation models, and species and content of the electrolyte (including Refs. [38–43]).

[38] C. Joseph, P. Bourson, and M. D. Fontana, Amorphous to crystalline transformation in Ta_2O_5 studied by Raman spectroscopy, J. Raman Spectrosc. **43**, 1146 (2012).

[39] W.-S. Liu, M.-W. Liao, S.-H. Huang, Y. I. A. Reyes, H.-Y. Tiffany Chen, and T.-P. Perng, Formation and characterization of gray Ta_2O_5 and its enhanced photocatalytic hydrogen generation activity, Int. J. Hydrogen Energy **45**, 16560 (2020).

[40] P. S. Dobal, R. S. Katiyar, Y. Jiang, R. Guo, and A. S. Bhalla, Raman scattering study of a phase transition in tantalum pentoxide, J. Raman Spectrosc. **31**, 1061 (2000).

[41] J. M. Casas, F. Alvarez, and L. Cifuentes, Aqueous speciation of sulfuric acid-cupric sulfate solutions, Chem. Eng. Sci. **55**, 6223 (2000).

[42] G. De Rijck and E. Schrevens, Elemental bioavailability in nutrient solutions in relation to dissociation reactions, J. Plant Nutr. **20**, 901 (1997).

[43] Colin Dawes, What is the critical pH and why does a tooth dissolve in acid?, J. Can. Dent. Assoc. **69**, 722 (2003).

[44] P. Skeldon, G. E. Thompson, G. C. Wood, X. Zhou, H. Habazaki, and K. Shimizu, Evidence of oxygen bubbles formed within anodic films on aluminium-copper alloys, Philos. Mag. **76**, 729 (1997).

[45] H. Habazaki, H. Konno, K. Shimizu, S. Nagata, P. Skeldon, and G. E. Thompson, Incorporation of transition metal ions and oxygen generation during anodizing of aluminium alloys, Corros. Sci. **46**, 2041 (2004).

[46] O. Kerrec, D. Devilliers, H. Groult, and P. Marcus, Study of dry and electrogenerated Ta_2O_5 and $Ta/Ta_2O_5/Pt$ structures by XPS, Mater. Sci. Eng. **B55**, 134 (1998).

[47] L. R. Marcus Textor, Rolf Hofer, Antonella Rossi, Kirill Feldman, Georg Hahner, and N. D. Spencer, Structural chemistry of self-assembled monolayers of octadecylphosphoric acid on tantalum oxide surfaces, Langmuir **16**, 3257 (2000).

[48] J. Li, W. Dai, G. Wu, N. Guan, and L. Li, Fabrication of Ta_2O_5 films on tantalum substrate for efficient photocatalysis, Catal. Commun. **65**, 24 (2015).

[49] K. V. Egorov, D. S. Kuzmichev, P. S. Chizhov, Y. Y. Lebedinskii, C. S. Hwang, and A. M. Markeev, *In situ* control of oxygen vacancies in TaO_x thin films via plasma-enhanced atomic layer deposition for resistive switching memory applications, ACS Appl. Mater. Interfaces **9**, 13286 (2017).

[50] W. Ren, G.-D. Yang, A.-L. Feng, R.-X. Miao, J.-B. Xia, and Y.-G. Wang, Annealing effects on the optical and electrochemical properties of tantalum pentoxide films, J. Adv. Ceram. **10**, 704 (2021).

[51] T. Heisig, K. Lange, A. Gutsche, K. T. Goß, S. Hambsch, A. Locatelli, T. O. Menteş, F. Genuzio, S. Menzel, and R. Dittmann, Chemical structure of conductive filaments in tantalum oxide memristive devices and its implications for the formation mechanism, Adv. Electron. Mater. **8**, 2100936 (2022).

[52] H. Kaftelen, K. Ocakoglu, R. Thomann, S. Tu, S. Weber, and E. Erdem, EPR and photoluminescence spectroscopy studies on the defect structure of ZnO nanocrystals, Phys. Rev. B **86**, 014113 (2012).

[53] D. G. Muth, Ellipsometer study of anodic oxides formed on sputtered tantalum and tantalum-aluminum alloy films, J. Vac. Sci. Technol. **6**, 749 (1969).

[54] F. Rubio, J. M. Albella, J. Denis, and J. M. Martinez-Duart, Optical properties of reactively sputtered Ta_2O_5 films, J. Vac. Sci. Technol. **21**, 1043 (1982).

[55] R. Swanepoel, Determination of the thickness and optical constants of amorphous silicon, J. Phys. E: Sci. Instrum. **16**, 1214 (1983).

[56] J. Sánchez-González, A. Díaz-Parralejo, A. L. Ortiz, and F. Guiberteau, Determination of optical properties in nanostructured thin films using the Swanepoel method, Appl. Surf. Sci. **252**, 6013 (2006).

[57] L. Khoroshko, A. Baglov, T. Orekhovskaya, S. Trukhanov, D. Tishkevich, A. Trukhanov, T. Raichenok, and A. Kopots, Optical properties of valve metals functional thin films obtained by electrochemical anodization on transparent substrates, Coatings **12**, 1678 (2022).

[58] E. Koushki and S. H. Mousavi, Periodic behavior of reflectance and transmittance from a thin film due to optical interference; the case of AlN nanostructure films, Surf. Interfaces **30**, 101821 (2022).

[59] M. Asnavandi, Y. Yin, Y. Li, C. Sun, and C. Zhao, Promoting oxygen evolution reactions through introduction of oxygen vacancies to benchmark NiFe-OOH catalysts, ACS Energy Lett. **3**, 1515 (2018).

[60] J. Wang, J. Liua, B. Zhang, F. Cheng, Y. Ruan, X. Ji, K. Xu, C. Chen, L. Miao, and J. Jiang, Stabilizing the oxygen vacancies and promoting water-oxidation kinetics in cobalt oxides by lower valence-state doping, Nano Energy **53**, 144 (2018).

[61] P. Yang, L. Wang, H. Zhuzhang, R. Wang, M.-M. Titirici, and X. Wang, Photocarving nitrogen vacancies in a polymeric carbon nitride for metal-free oxygen synthesis, Appl. Catal. B **256**, 117794 (2019).

[62] Y. Tong, H. Mao, Y. Xu, and J. Liu, Oxygen vacancies confined in Co_3O_4 quantum dots for promoting oxygen evolution electrocatalysis, Inorg. Chem. Front. **6**, 2055 (2019).

[63] A. Rajapriya, S. Keerthana, A. Rebekah, C. Viswanathan, and N. Ponpandian, Enriched oxygen vacancy promoted heteroatoms (B, P, N, and S) doped CeO_2: Challenging electrocatalysts for oxygen evolution reaction (OER) in alkaline medium, Int. J. Hydrogen Energy **46**, 37281 (2021).

[64] W.-J. Chun, A. Ishikawa, Tsuyoshi Takata, Hideki Fujisawa, Michikazu Hara, Junko N. Kondo, Maki Kawai, Yasumichi Matsumoto, and Kazunari Domen, Conduction and valence band positions of Ta_2O_5, TaON, and Ta_3N_5 by UPS and electrochemical methods, J. Phys. Chem. B **107**, 1798 (2003).

[65] V. Y.-Q. Zhuo, Y. Jiang, M. H. Li, E. K. Chua, Z. Zhang, J. S. Pan, R. Zhao, L. P. Shi, T. C. Chong, and J. Robertson, Band alignment between Ta_2O_5 and metals for resistive random access memory electrodes engineering, Appl. Phys. Lett. **102**, 062106 (2013).

[66] L. Yang, Y. Yang, J. R. Lombardi, Y. Peng, and Z. Huang, Charge transfer enhancement in the surface-enhanced Raman scattering of Ta_2O_5 superstructures, Appl. Surf. Sci. **520**, 146325 (2020).

[67] C. J. C. Aleksandr, V. Marenich, and Donald G. Truhlar, Universal solvation model based on solute electron density and on a continuum model of the solvent defined by the bulk dielectric constant and atomic surface tensions, J. Phys. Chem. B **113**, 6378 (2009).

[68] T. Lu and F. Chen, Multiwfn: A multifunctional wavefunction analyzer, J. Comput. Chem. **33**, 580 (2012).

[69] A. D. William Humphrey and K. Schulten, VMD: Visual molecular dynamics, J. Mol. Graphics **14**, 33 (1996).